ORIGINAL PAPER

RETROFITTING OUTDATED PYRANOMETER FOR IoT INTEGRATION TOWARDS A CIRCULAR ECONOMY MODEL

VIOREL MIRON-ALEXE[1], GABRIELA MANTESCU[1]

Manuscript received: 18.05.2023; Accepted paper: 06.11.2023;
Published online: 30.12.2023.

Abstract. *An innovative way of applying the circular economy concept in the obsolete research equipment domain is by repairing and upgrading critical subcomponents of the initial equipment, for reuse purposes. Thus, a large percentage of environmental waste is reduced, resulting from the whole process of manufacturing a brand new modern one, along with the implied purchasing costs, while serving its intended purpose simultaneously. The whole re-engineering process produces increased overall cost efficiency, by massively reducing the raw material requirements, the electrical energy consumption for design and manufacture, and the resulting waste material. In this respect, the article addresses the inherent issues in retrofitting an old model analog signal pyranometer, designed in the '90s. The upgrade initiative aims to massively increase the digital processing speed, the quality, and the quantity of the data acquisition, while also providing an integrated local storage solution and wireless access through a designated IP address using a web interface, for data interrogation in real-time. All these are done at low costs, with market-available materials, to avoid any high expenses related to acquiring new ones.*

Keywords: *thermopile pyranometer; solar irradiance sensor; IoT embedded system; web chart real-time wireless server; CSV data logger.*

1. INTRODUCTION

The present article highlights the upgrading possibility with new technology, of old but valuable research devices, by genuinely contributing to the global circular economy paradigm, while also achieving low costs and low energy consumption, innovatively, when multidisciplinary know-how is correctly applied. Although it is not exactly a new concept, equipment retrofitting has been around since the dawn of the industrial age, being implemented starting from the mechanical modules of machines such as military and medical hardware, industrial machinery, scientific equipment, civilian household devices, and so on; to the ubiquitous firmware and software-based electronic devices, present in every aspect of our lives.

In analogy to that, and judging by the circular economy system, the upgrade with a digital interface of old research analog hardware, can bring important benefits for all the engaged parts. These advantages are especially on the financial side, but also on the technological side which can better serve in the data acquisition process, which is paramount in the research area.

[1] Valahia University of Targoviste, Institute of Multidisciplinary Research for Science and Technology, Energy and Environment Research Department, 130004 Targoviste, Romania. E-mail: viorel.alexe@protonmail.com; gabriela.mantescu@yahoo.com.

https://doi.org/10.46939/J.Sci.Arts-23.4-c02

In this regard, the candidate subjected to the experimental digital upgrade was a salvaged pyranometer found in a poor condition, that was not operational by any means. The main issues identified were the defective acquisition and control circuit board, as well as the inexistent power and data hybrid cable, that would have connected the actual pyranometer sensor unit to the acquisition and control unit. Usually, in this kind of situation the equipment would most probably be discarded or recycled, just to be replaced with a new one.

To apply the circular economy paradigm over a retrofitting technical procedure, an oversimplified diagram with five major steps was considered, as described in Fig. 1:

- **Reevaluating** the remaining components of the old device to assess which one is functional or repairable and suited for the upgrade procedure.
- **Reengineering** and compatibilization by implementing new components, modifying the original components that need the digital upgrade, or reconstruction of the missing needed components.
- **Retesting** the device in a simulated environment to assess the input and output parameters, with the inherent hardware, firmware, and software modifications or improvements.
- **Recalibrating** the reconstructed and upgraded device within the original technical parameters, by mechanical, electrical and software means.
- **Reusing** the upgraded device in the natural environment by observing its behavior while acquiring and analyzing the output data.

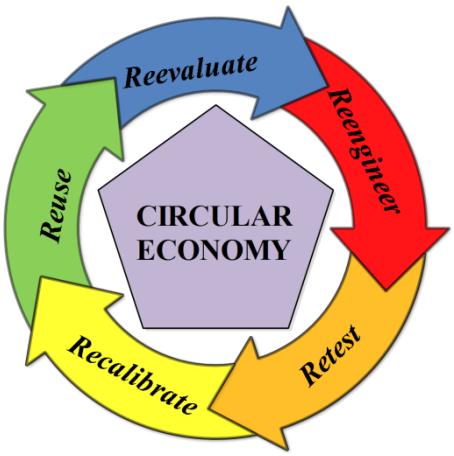

Figure 1. Circular economy diagram pointing to the major steps used in retrofitting the pyranometer.

Unsurprisingly as in any reengineering process, the steps were often interchanged and repeated multiple times, to have a fully functional prototype. After various measurement sessions of solar irradiance, the finished pyranometer prototype checked the requirements of the initial goal from the start of the experimental retrofitting plan, such as performant IoT embedded system with offline wireless AP and file-server ability; real-time data point chart display on an HTML page with a saving options menu; CSV datalog on SD-Card storage with RTC for recording each data point event time; on/off, reset, ventilation, and heating button control on the frontal console; accurate measurement and manual sensitivity calibration option; real-time data value and time display on an illuminated background LCD; user-friendly and fast deployment.

2. STATE OF THE ART

Commercially, there are two types of technologies used in pyranometers (1) the older technology is based on thermopile sensors, and (2) the newer technology is based on semiconductor sensors. Due to the way they are engineered, the thermopile pyranometers exhibit a slower response time to the variations of external environmental factors (solar irradiance and temperature), while acquiring a small number of measurements over a longer timespan, thus having a smoother transition between the data points [1]. On the other hand, the semiconductor pyranometers exhibit a faster response time, while acquiring a large quantity of measurements over a shorter timespan, thus having a sharper transition between the data points, but being more prone to the external stray spectral noise. Of course, depending on the technology used in solar irradiance measurements, different spectral sensitivity and spectral response are obtained accordingly [2]. Fig. 2 presented a generic graph with the spectral irradiance response at different wavelengths, of a thermopile-based pyranometer versus two semiconductor-based pyranometers.

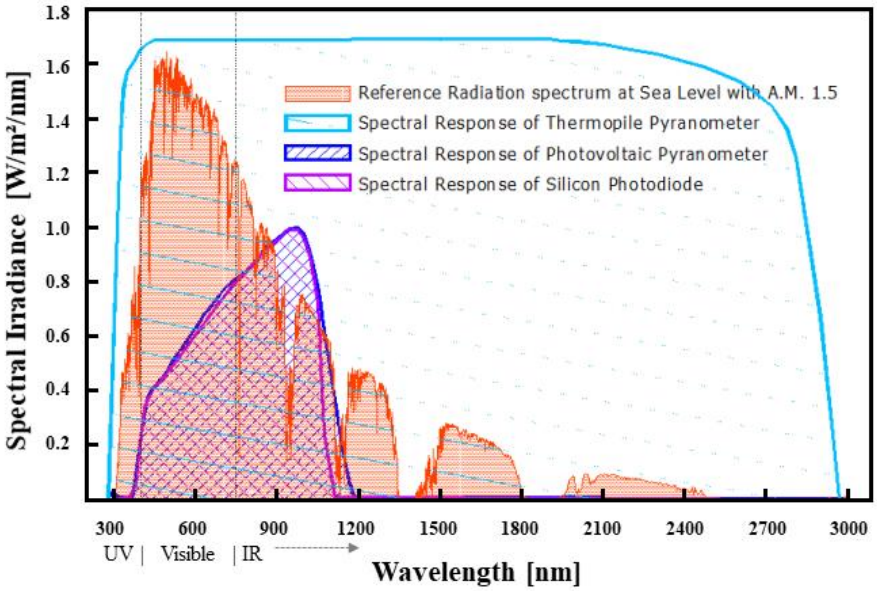

Figure 2. Graph with the spectral irradiance response of three types of pyranometers [3].

As can be observed in the comparative measurement graph, the thermopile pyranometer has a broader solar spectrum but a different spectral response compared to the semiconductor pyranometers (photovoltaic and photodiode). More relevant comparative technical specifications and differences of the two types of pyranometers are presented in Table 1. While the thermopile pyranometers are generally more suited for meteorological measurements, the semiconductor ones are more suited for the estimation of photovoltaic installations power output, or as reference cells in laboratory measurements, because of the matching semiconductor spectral response and spectral range.

Table 1. Generic technical comparison between thermopile and semiconductor pyranometers.

Pyranometer's main technical parameters	Unit	Thermopile pyranometer typical values	Semiconductor pyranometer typical values
Spectral range	[nm]	300-2800	350-1150
Response time	[s]	<30	<0.001
Sensitivity	[μV/Wm^2]	<20	<2500
Temperature	[°C]	-40 to +50	-40 to +65

The sensor unit used in this research was taken from an old CM21 series pyranometer, which was primarily designed to measure the Global Horizontal Irradiance (GHI), which is the total solar irradiance incident on a fixed horizontal surface, which is derived from the Direct Normal Irradiance (DNI) coming from the Sun, combined with the Diffuse Horizontal Irradiance (DHI) coming from the Earth's hemisphere. The GHI, the DNI, and the DHI are solar energy measurement parameters that are used in photovoltaic systems and meteorological weather stations [4].

On a brief inspection of the evaluated CM21 device and according to the technical datasheet [5], the type of sensing element is a thermopile-based one that creates a voltage potential between the black-coated sensing plate and the compensation plate, because of thermal differences that occur between the two different material elements. Also, the sensor of the pyranometer is advertised by the manufacturer as one with high sensitivity and low impedance, low-temperature response, and low nonlinearity. Fig. 3 describes a cross-section of a typical thermopile pyranometer and its constructive components that resemble the CM21 one.

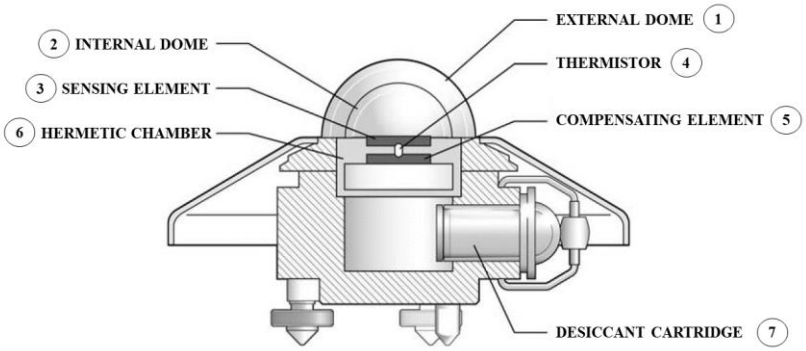

Figure 3. Thermopile pyranometer cross-section and its constructive components as follows: 1-external glass dome; 2-internal glass dome; 3-sensing element; 4-thermistor; 5-compensating element; 6-hermetic chamber; 7-desiccant cartridge [6].

The extracted technical data of the CM21 pyranometer unit used in the retrofitting experiment is presented in Table 2.

Table 2. CM21 pyranometer specs. according to ISO 9060.

Main technical parameters	Unit	Value	Additional information
Spectral range	[nm]	335-2200	95% points
Sensitivity	[μV/Wm^2]	7-17	N/A
Impedance	Ω	40-100	N/A
Response time	[s]	5	95% response
Operating temperature	[°C]	-40 to +80	N/A
Nonlinearity	[%]	<±0.2	<1000 W/m^2
Spectral selectivity	[%]	<±2	N/A
Temp. dependence of sensitivity	[%]	<±1	-20°C to +50°C
Directional error	[W/m^2]	<±10	beam 1000 W/m^2
Tilt error	[%]	<±0.2	beam 1000 W/m^2
Zero offset due to FIR	[W/m^2]	<7	at 200 W/m^2 net radiation
Zero offset due to temperature variations	[W/m^2]	<2	at 5 K/h temperature change

Given the fact that the presented thermopile pyranometer itself was a few decades old, there was a 100% chance that the sensitivity had changed and thus the original calibration was lost, due to the physical aging of the materials that the sensor and the thermal compensation

circuit were built of. Fig. 4 presents the actual CM21 pyranometer unit without the shielding cover.

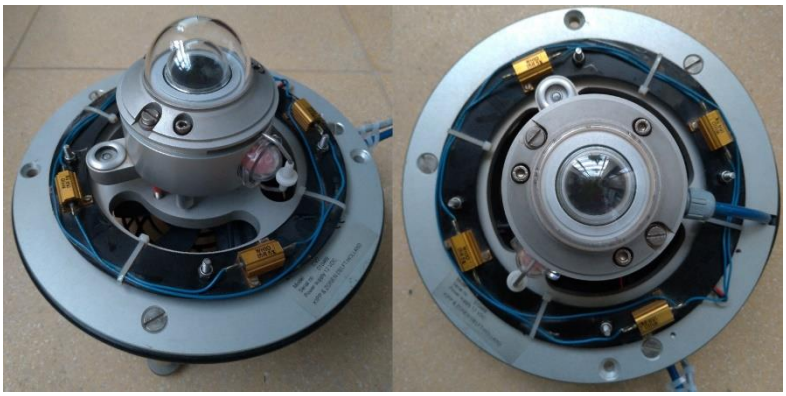

Figure 4. CM21 pyranometer unit without the top cover.

As observed, the composing elements of the device are the exposed aluminum sensing module with the double glass dome, the surrounding heating resistor array, the underneath positioned blowing fan, the desiccant cartridge, and the bubble leveler. The unit is manually adjustable on a plane surface for the *x* and *y* axis, by using the screwed tripod feet from the frame and the bubble leveler.

3. RESULTS AND DISCUSSION

By further analyzing the technical documentation and the components inside the actual CM21 pyranometer unit, it is acknowledged that the sensing module is a standalone analog one, assisted by a thermal compensation circuit with two NTC thermistors. Thus, any digital conversion and processing is done separately by the acquisition and control unit on the other end of the cable, as described in Fig. 5.

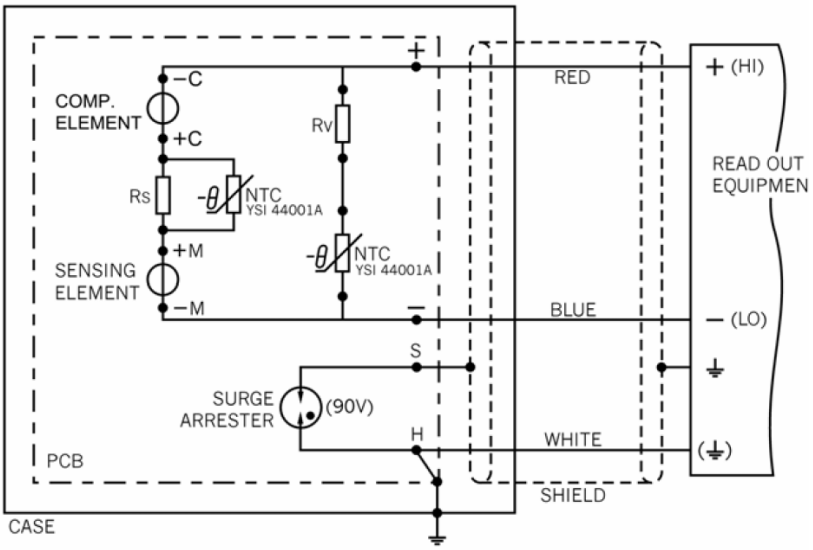

Figure 5. Electrical diagram of the analog pyranometer sensing module with internal thermistor-based thermal compensation circuit and static discharge protection [7].

On the other hand, the defective acquisition and control unit contained a multitude of dedicated digital subcircuits for the pyranometer heating and ventilation control, DC voltage regulation and logic supply voltage conversion, logic multiplexing, programmable voltage reference, analog to digital conversion, LCD and RS232 serial communication functions.

Thus, the proposed reengineering process of the whole pyranometer included two main upgrade aspects: (1) an integrated digital conversion module that can assert multiple sensor-specific functions, which is encased in the aluminum chamber of the pyranometer unit, and (2) a redesigned acquisition and control unit with multiple complex functions.

In the retrofitting process, aside from the standalone thermopile analog sensor, the whole pyranometer has undergone massive hardware transformations to facilitate large amounts of data acquisition, processing access and storage, and multi-client wireless server connectivity in real time. Thus, for a better comprehension of the global redesign initiative of the device, a comparative subcomponent block diagram is presented in Fig. 6. The orange upper layout section represents the former design of the analog pyranometer which is a very basic setup, while the green lower layout section represents the upgraded design proposed by the author.

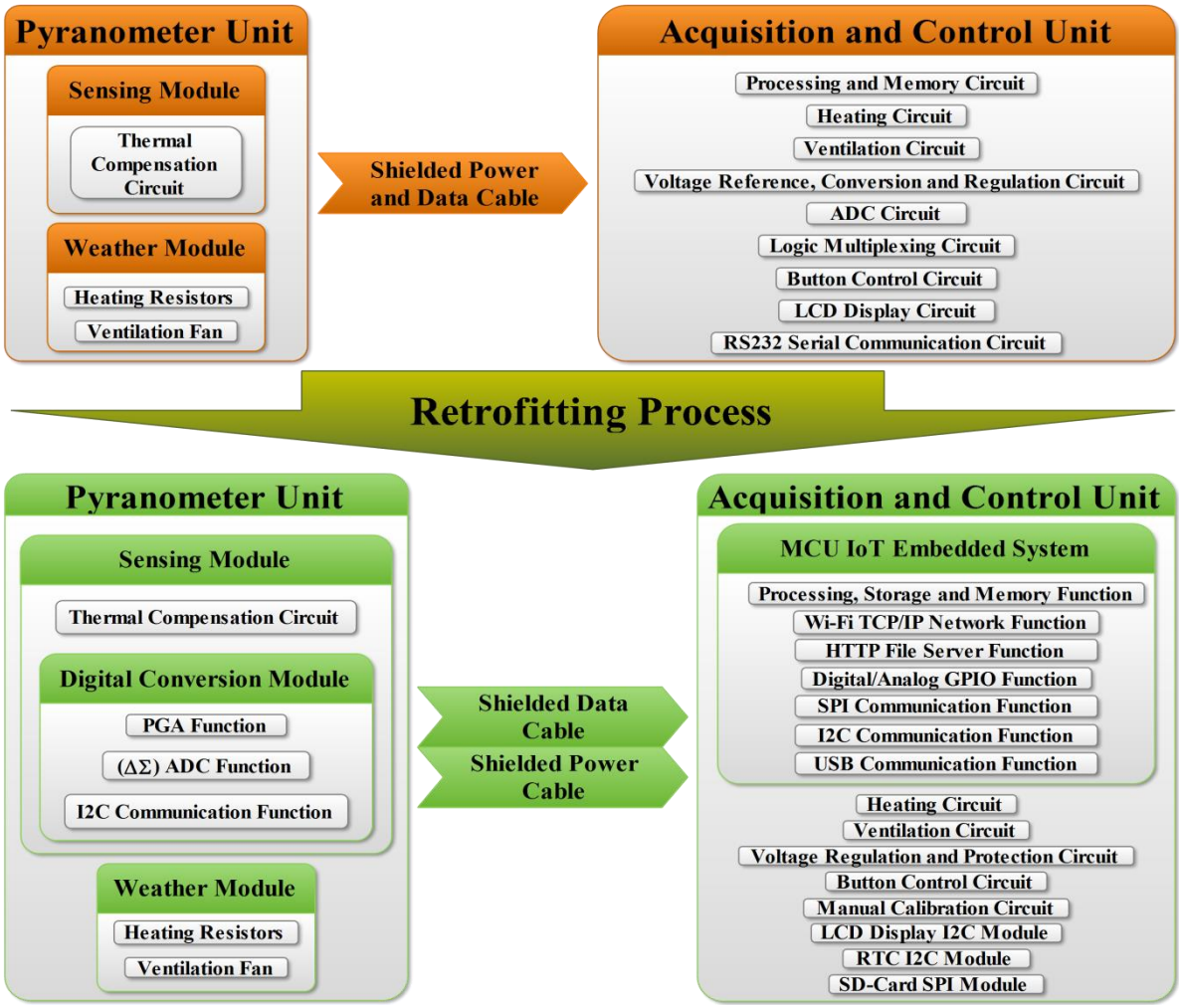

Figure 6. Subcomponent block diagram of the former pyranometer design (orange), versus the proposed reengineered subcomponent design (green).

The pyranometer unit was also upgraded with a performant „*in situ*" 12-bit PGA (Programmable Gain Amplifier) based (ΔΣ) ADC module, to convert the analog signal from the thermopile sensing module into a digital one, while shielding it against any local

interference. Another advantage of using this proposed „in situ" digital signal conversion and transmission technique is that the wire resistance and external EMI or ESD noises are eliminated. Thus, any former compensation and protection circuits from the acquisition and control unit side are excluded from use. This shielding method is reflected in the quality of the signal and therefore the accuracy of the data acquisition.

The novelty of this research is related to that the digital conversion module from the pyranometer unit can communicate by I2C protocol with the MCU IoT embedded system and the other modules from the acquisition and control unit, through a 5-meter shielded data cable with 0 data package loss. Further technical details about this specific subject will remain undisclosed for obvious reasons, while trials for an extended cable communication distance are under scientific scrutiny. Fig. 7 depicts the entire modified pyranometer, in a set of four subfigures, best describing the pyranometer sensing unit (1) and the pyranometer acquisition and control unit, with exterior (2) and interior (3) and (4) presentation. As can be observed, the pyranometer sensing unit is comprised of the exposed sensor glass domes, a white aluminum shield with the weather module, the sensing module with the thermal compensation circuit and digital conversion module, and the solid aluminum frame, all underneath it.

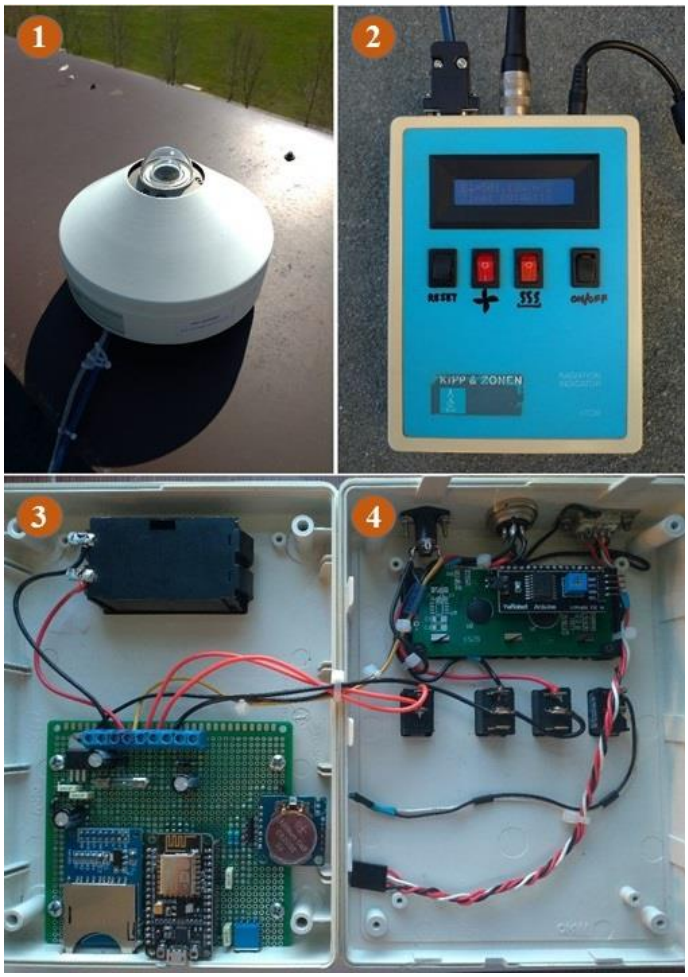

Figure 7. Retrofitted pyranometer photographic depiction as 1-pyranometer sensing unit; 2-pyranometer acquisition and control unit (exterior); 3 and 4-pyranometer acquisition and control unit (interior).

The pyranometer acquisition and control unit is comprised, on the exterior, of the button control console (reset button, ventilation button, heating button, and ON/OFF button), the LCD with real-time solar irradiance value and time, and the connector console; while on the interior, it is comprised of the programmed MCU IoT embedded system, RTC module,

SD-Card module, LCD module and the rest of the circuits already described in the retrofitting process subcomponent block diagram.

The general theoretical way of calculating the GHI is by the relation (1):

$$GHI = DHI + DNI \times \cos(z) \tag{1}$$

where *GHI* is the Global Horizontal Irradiance, *DHI* is the Diffuse Horizontal Irradiance, *DNI* is the Direct Normal Irradiance, and *cos(z)* is the zenith incidence angle of the Sun over a flat surface.

A theoretical adaptation to relation (1), for computing the global irradiance value by a typical analog pyranometer configuration is provided as (2), which is also found in the technical datasheet:

$$E_{\downarrow} = \frac{U_{th}}{U_{sens}} \tag{2}$$

where $E_{\downarrow}$ is the global irradiance value expressed in [W/m^2], U_{th} is the analog value of the thermopile sensor expressed in [µV], and U_{sens} is the sensitivity of the pyranometer expressed in [µV/Wm^2].

Although more details about the algorithm programmed in the MCU IoT embedded system will remain undisclosed in this article, a purely theoretical calculus is proposed for the digitalized thermopile signal in the re-engineered configuration.

Thus, the U_{th} analog signal is at first amplified by the PGA, resulting in (3):

$$U_{th'} = U_{th} \times PGA_{val} \tag{3}$$

where $U_{th'}$ is the amplified analog signal of U_{th} while PGA_{val} is the 8 times amplification ratio of the PGA.

Integrating (3) in the ADC calculation formula, a new relation is generated as (4):

$$ADC_{val} = U_{th'} \times \frac{ADC_{res}}{V_{ref}} \tag{4}$$

where ADC_{val} is the calculated ADC numeric value, ADC_{res} is the 12-bit resolution of the ADC or 2^{12} numeric value, and V_{ref} is the 3.3 V reference voltage of the ADC module.

Merging relations (3) and (4), a complete calculation formula is computed to express $E_{\downarrow}$, thus relations (5), (6), and (7) are elaborated:

$$E_{\downarrow} = \frac{\left(U_{th} \times PGA_{val}\right) \times ADC_{val}}{U_{sens}} \tag{5}$$

$$E_{\downarrow} = \frac{\left(U_{th} \times PGA_{val}\right) \times \frac{ADC_{res}}{V_{ref}}}{U_{sens}} \tag{6}$$

$$E_{\downarrow} = \frac{U_{th'} \times \frac{ADC_{res}}{V_{ref}}}{U_{sens}} \tag{7}$$

Finally after (7) is calculated and reduced, it becomes (8):

$$E_{\downarrow} = \frac{U_{RAW}}{U_{sens}} \times 10^3 \tag{8}$$

where U_{RAW} is the numeric output voltage value of the digital conversion module, expressed in mV, which is proportional to the input signal value of the pyranometer sensing module. As a small observation, the PGA-ADC digital conversion module can amplify, filter, and convert the thermopile analog input signal, into a digital numeric value output signal, with only a 0.2% error tolerance.

An important aspect of the pyranometer retrofitting is the ratiometric calibration procedure that was conducted using the pyranometer and an online current weather and forecasting server (Solcast), on a clear weather condition and peak Sun hours day, at a designated GPS location. As a result, the sensitivity value of U_{sens} for the exterior measurements was manually adjusted to 17 µV/Wm^2, which is within the upper sensitivity limit of the CM21 pyranometer stated in Table 2.

Figure 8. Demonstrative measurement live session chart with GHI (red) and RAW (blue) data values.

In the early stages of device observation and testing, multiple solar irradiance measurements were conducted while the streaming data was captured on a smartphone wirelessly connected to the redesigned pyranometer. Thus in Fig. 8 it is presented a demonstrative offline measurement session during a late spring day (partly cloudy sky), rendered as two synchronized data point charts in a 25 minutes timespan, on a web page of a mobile phone. The red upper chart represents each calculated digital value for the GHI expressed in W/m^2, while the blue lower chart represents the RAW output sensor value expressed in mV.

Given the fact that the GHI measurements can be somewhat relative, depending on the equipment used, local setup and calibration, local weather, and other local physical factors, and although the prototype lacked standardized ISO, IEC, and WMO calibration [8], some relevant results were still obtained. Furthermore as a proof of concept, (Fig. 9) depicts a 10-day GHI value chart capture from the Solcast website at the same GPS coordinates, which also includes a past registration for 23-May-2023 (arrow highlighting the GHI computed value registered at 1:00 PM), when a parallel measurement session with the manually calibrated pyranometer was also made.

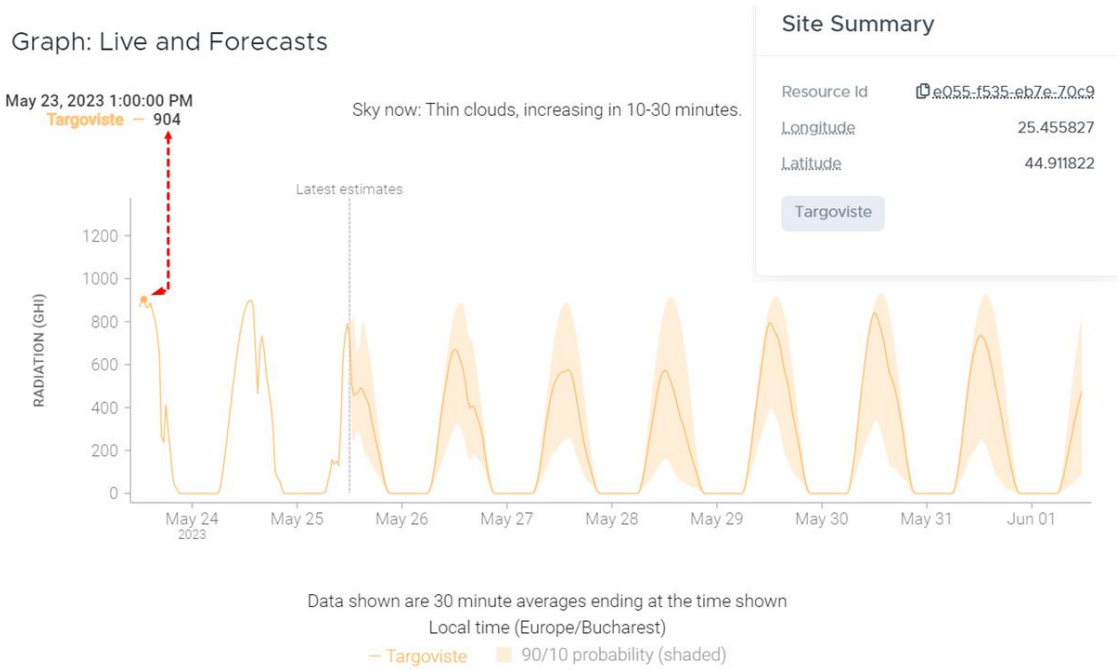

Figure 9. Solcast server daily GHI chart with the red dotted arrow pointing to value, location, and date.

Finally, a full comparative report for GHI values between the measurements from the retrofitted pyranometer and the Solcast online forecasting server, was also generated from the CSV files, in the form of a graph presented in (Fig. 10). The report covers 6 hours intervals starting from 9:00 AM to 3:00 PM, with a data point granularity of 5 minutes interval.

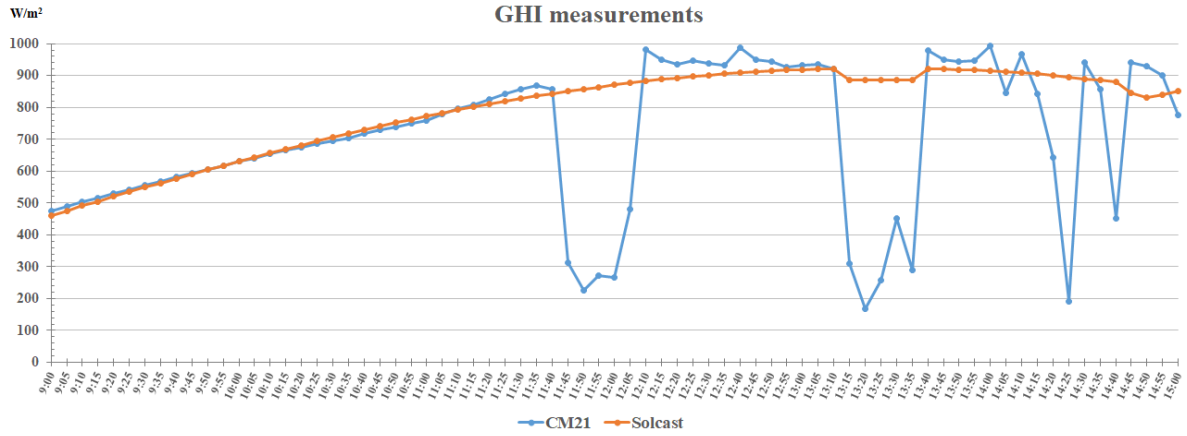

Figure 10. Comparative GHI report between CM21 reengineered pyranometer and Solcast server in the 9:00 AM and 3:00 PM interval.

As expected, by analyzing the comparative graphs, the pyranometer acquired GHI data (blue) and exhibited a pronounced variation due to the dynamics of the local clouds and the lens effect generated when sunlight passed through them. Aside from the falling spike values,

a certain degree of matching linearity is maintained with the Solcast registered values (orange), in the distribution of the data points within the 9:00 AM and 11:40 AM interval. To make a full qualitative and quantitative evaluation of the pyranometer data in the outside weather testing conditions, some specific criteria need to be met, such as at least 14 hours/day of undisrupted measurement of GHI on an all-clear weather day (for May), a measurement session for an entire month/season/year, and positioning of the pyranometer on a flat and clear terrain. Although not all the mentioned criteria were met, there was still enough gathered data to make a qualitative comparative scrutiny (Fig. 11).

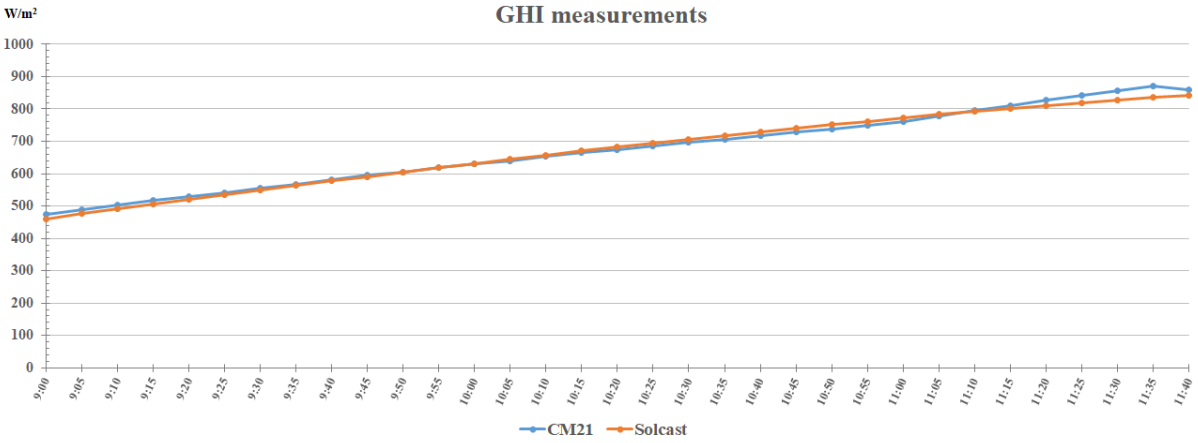

Figure 11. Comparative GHI report between CM21 reengineered pyranometer and Solcast server in the 9:00 AM and 11:40 AM interval.

Consequently, for modeling the data sets from the re-engineered CM21 pyranometer (observed values) and the Solcast server (simulated values), in the 9:00 AM and 11:40 AM intervals, several comparative statistical calculus methods have been used [9].

Thus, to calculate the root mean square error (*RMSE*), relation (9) is generated:

$$RMSE = \sqrt{\frac{\sum_{i=1}^{n}\left(X_{obs,i} - X_{sim,i}\right)^2}{n}} \tag{9}$$

where $X_{obs,i}$ is the observed sample value of the pyranometer, $X_{sim,i}$ is the simulated sample value of the Solcast sever, and n is the number of data points.

Computing the two data sets using (9), a linear regression graph is performed in Fig. 12.

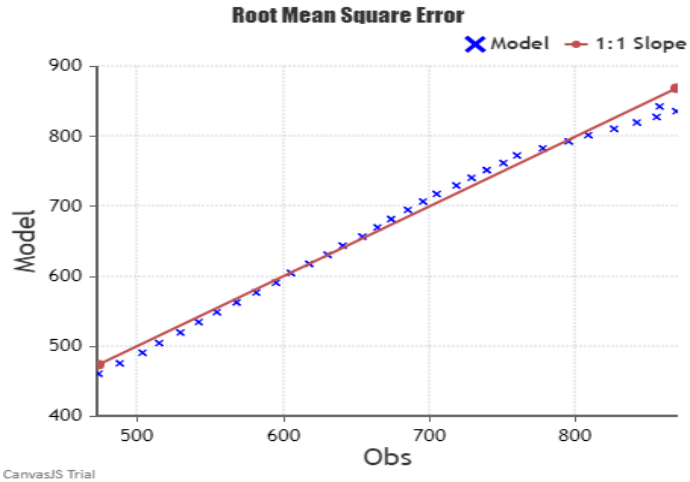

Figure 12. RMSE of two combined data sets versus linear regression model.

To calculate the normalized root mean square error (*NRMSE*), relation (10) is generated:

$$NRMSE = \frac{RMSE}{\overline{X_{obs,i}}} \tag{10}$$

where $\overline{X}_{obs}$ is the mean value of the pyranometer data set.

To calculate the mean bias error (*MBE*), relation (11) is generated:

$$MBE = \frac{1}{n}\sum_{i=1}^{n}\left(X_{sim,i} - X_{obs,i}\right) \tag{11}$$

To calculate the Pearson correlation coefficient (*r*), relation (12) is generated:

$$r = \frac{\sum\left(X_{obs,i} - \overline{X_{obs}}\right)\left(X_{sim,i} - \overline{X_{sim}}\right)}{\sqrt{\sum\left(X_{obs,i} - \overline{X_{obs}}\right)^2 \sum\left(X_{sim,i} - \overline{X_{sim}}\right)^2}} \tag{12}$$

where *r* is the Pearson's correlation coefficient, $X_{obs,i}$ is the observed sample value of the pyranometer, $X_{sim,i}$ is the simulated sample value of the Solcast sever, $\overline{X}_{obs}$ is the mean value of the pyranometer data set, and $\overline{X}_{sim}$ is the mean value of the Solcast sever data set.

Table 3. summarizes the calculus results of (9), (10), (11), and (12) relations for the two data sets.

Table 3. Calculus results for the pyranometer and the Solcast data sets.

Calculation method	Unit	Calculated value
RMSE	[W/m^2]	12.29
NRMSE	[%]	0.018
MBE	[W/m^2]	-2.78
Pearson correlation coefficient	[%]	0.989

From Table 3 it can seen, that the calculated percentage value of NRMSE is almost negligible, as well as the calculated percentage value of Pearson's correlation coefficient, which has a positive matching correlation in the same direction toward unity. Also, a slightly negative estimation value is observed in the MBE result, as well as an acceptable positive estimation value in the RMSE result. The overall analysis of the results from the two data series, found in Table 3, promotes the idea that the retrofitted pyranometer is accurate enough to conduct GHI measurements within acceptable error tolerances and that the present sensitivity calibration value, is correctly adjusted within a safe margin. Also, as a side note, during the GHI measurement trials, a parallel power consumption measurement was conducted on the retrofitted pyranometer, for each case. Thus, in a humid cold weather scenario, the weather module was enabled to clear the thermopile dome surface from dust, dew, and fog, registering a power draw of 15.3 Wh. While in a warm weather scenario with no persisting humidity, the weather module was disabled, registering a power draw of only 1.9 Wh. As a small mention, in both cases, the Wi-Fi function was active.

4. CONCLUSIONS

As observed in the previous comparative report from Fig. 10, the online current weather and forecasting Solcast server could not correctly model the whole GHI value dataset, obtaining a mostly normalized distribution curve of the GHI data points, with almost no regard for the cloud variations, in the partly cloudy sky scenario. The CM21 reengineered pyranometer being installed on a ground level, also captured the light variations when passing clouds blocked the sunlight that reached the sensor. On the other hand, as can be observed from the comparative report (Fig. 11), both the Solcast server and the redesigned pyranometer, acquired very similar GHI values, for the clear weather scenario of the initial GPS location measurement site.

Corroborating the two observations, several conclusions are drawn. The first is related to the re-engineered pyranometer that obtained almost similar GHI data points compared with the Solcast server GHI data points, for the clear weather scenario. Thus the theoretical and empirical calibration of the CM21 reengineered pyranometer, were precise and within the stated datasheet technical values. The second conclusion is that from the research perspective, it is always best for any observed parameter to simultaneously be measured by multiple sources or tools. This way, the abundance of data can help to conduct a more elaborate research scrutiny. Such tools can be represented by official local weather stations combined with online forecasting and nowcasting weather servers or other third-party online weather stations, which can export weather data reports. The third one is that not all of the online weather tools can offer a fully precise weather report based on a local GPS map point, but they can only offer a general weather perspective on an extended region and time. The fourth conclusion is that to increase the resolution and precision of the weather-acquired data for multiple smaller regions of interest, a mesh of deployable, interlinked, remote, IoT weather stations, would offer a broader and more accurate local weather report.

Finally, further research directives can include the merging of technologies between nowcasting and forecasting online weather data servers, and locally, deployable, IoT weather stations, for better results. Also, further calibration and accuracy improvements can be implemented on the software side to eliminate data disruptions according to studies revealed by Azouzoute et al. [10] and Mubarak et al. [11].

REFERENCES

[1] Karki, S., Ziar, H., Korevaar, M., Bergmans, T., Mes, J., Isabella, O., *IEEE Journal of Photovoltaics*, **11**, 144, 2021.
[2] Zeqiang, B., Wenhua, L., Yizhuo, S., Xiaolei, H., Wei, C., *2013 IEEE 11th International Conference on Electronic Measurement & Instruments*, **1**, 43, 2014.
[3] https://www.myussi.com/glossary/pyranometer/.
[4] https://toolkit.solcast.com.au/legacy-live-forecast.
[5] https://solrad-net.gsfc.nasa.gov/cm21.pdf.
[6] Rahman, M.M., Zhang, W., *Journal of Earth System Science*, **128**, 84, 2019.
[7] https://archive.eol.ucar.edu/docs/isf/facilities/isff/sensors/kippzonen/manual_cm21.pdf.
[8] Zerlaut, G. A., *Solar Radiation Measurements: Calibration and Standardization Efforts*, Springer, Boston, 42, 1983.
[9] Gueymard, C. A., *Renewable and Sustainable Energy Reviews*, **39**, 1024, 2014.

[10] Azouzoute, A., Merrouni, A. A., Bennouna, E. G., Gennioui, A., *Energy Procedia*, **157**, 1202, 2019.
[11] Mubarak, R., Schilke, H., Seckmeyer, G., *Energies*, **14**, 2766, 2021.